

Article

A Nickel-Based Coordination Compound with Tunable Morphology for High-Performance Anode and the Lithium Storage Mechanism

Yifei Lu [†], Lei Wang [†], Zhenzhu Lou [†] , Leilei Wang, Yi Zhao, Weiwei Sun, Liping Lv, Yong Wang 
and Shuangqiang Chen ^{*} 

Department of Chemical Engineering, School of Environmental and Chemical Engineering, Shanghai University, Shangda Road 99, Shanghai 200444, China; lyf19722737@shu.edu.cn (Y.L.)

^{*} Correspondence: chensq@shu.edu.cn; Tel.: +86-21-66136598

[†] These authors contributed equally to this work.

Abstract: Metal-organic coordination compounds (MCCs) have received a lot of attention as anodes for lithium-ion batteries (LIBs) due to their abundant structural configuration, tunable morphology, high surface area, and low cost, but the lithium storage mechanism of MCCs is still a mystery. Herein, we synthesized a kind of nickel-based coordination compound (marked as Ni-PP-*x*, *x* = 1, 2, or 3) with tunable morphologies and different solvent ratios via a microwave irradiation solvothermal method and then applied them as anodes for LIBs. Among them, the Ni-PP-2 electrode, with a hollow and urchin-like structure, showed the longest lifespan and maintained a high capacity of 713 mAh g⁻¹ at 2.0 A g⁻¹ after 800 cycles. Measured by ex situ X-ray photoelectron spectroscopy (XPS) and ex situ Fourier transform infrared spectroscopy (FT-IR), the Ni-PP-2 electrode was confirmed by a redox reaction mechanism of Li⁺ cations with a benzene ring and O-Ni²⁺/O-Ni⁰ coordination bonds, and the cyclic voltammetry curves have exhibited a capacitive dominated lithium storage behavior. This work provides a new type of Ni-based coordination compound and an in-depth understanding of their lithium storage mechanism, paving the way for the application of MCC compounds in the future.

Keywords: Ni-based coordination compounds; lithium-ion batteries; Li-storage mechanism; ex situ measurement techniques



Citation: Lu, Y.; Wang, L.; Lou, Z.; Wang, L.; Zhao, Y.; Sun, W.; Lv, L.; Wang, Y.; Chen, S. A Nickel-Based Coordination Compound with Tunable Morphology for High-Performance Anode and the Lithium Storage Mechanism. *Batteries* **2023**, *9*, 313. <https://doi.org/10.3390/batteries9060313>

Academic Editor: Catia Arbizzani

Received: 30 March 2023

Revised: 29 May 2023

Accepted: 3 June 2023

Published: 6 June 2023



Copyright: © 2023 by the authors. Licensee MDPI, Basel, Switzerland. This article is an open access article distributed under the terms and conditions of the Creative Commons Attribution (CC BY) license (<https://creativecommons.org/licenses/by/4.0/>).

1. Introduction

With the benefits of high energy density, long cycle life, and low self-discharge rate, lithium-ion batteries (LIBs) are widely utilized in portable electronic devices, electric vehicles, aerospace, etc. [1,2]. The electrochemical performance of LIBs is mainly influenced by the capacity and operating potential of the electrode materials. Graphite, the most common commercial anode material, has a theoretical capacity of 372 mAh g⁻¹ but it is gradually incapable of meeting the energy market's growing demand for battery energy density, so it is pressing to develop new types of materials with high capacity, superior rate capability, and low cost. Recently, carbon-based materials such as silicon, germanium, metal alloys, and transition metal oxides/sulfides have undergone extensive research as anode materials for LIBs based on different design strategies, including surface modification, ion doping, structural adjustment, and carbon recombination. However, these anode electrode materials are still struggling with many issues, such as significant volume changes, sluggish ionic transportation, and poor conductivity, which lead to significant capacity fading and unstable cycle behavior [3–5]. Thus, it is crucial to create functional anode materials with high capacity, excellent mechanical stability, and superior cyclability. Organic-based materials (conductive polymers, organic sulfides, metal/covalent organic frameworks, etc.) have fascinating potential as anode materials for the development of LIBs,

as they have good features of structural diversity, tunable morphology, a simple synthesis process, and renewable resources, showing many advantages over those aforementioned inorganic materials.

Metal-organic coordination compounds (MCCs), a type of organic material coordinating metal cations as central atoms and organic ligands as linkers, provide copious candidates with tunable features and low cost for anodes of LIBs [6,7]. Most prominently, MCCs offer rich and steady channels for ion migration during charging and discharging processes with tunable morphologies (including one-dimensional chains, two-dimensional layers, and three-dimensional frameworks), high specific surface area, and rich active sites [8,9]. As a result, the reported MCCs as anode materials have exhibited astounding electrochemical performance due to their robust oxidation-reduction reaction capability and multi-electron reaction process. In 2006, Li et al. evaluated the lithium storage performance of $\text{Zn}_4\text{O}(\text{1,3,5-benzenetricarboxylate})_2$ (MOF-177) material as an anode, which gave a relatively high initial discharge capacity of 400 mAh g^{-1} at 0.05 A g^{-1} . Although MOF-177 does not exhibit satisfactory cycle stability, it has established a strong foundation for applying MCCs to LIBs [10]. Subsequently, a variety of different MCC anode materials are reported by altering the kinds of metal ions and organic ligands, such as $\text{Zn}_3(\text{HCOO})_6$ [11], $[\text{Pb}(\text{4,4'-ocpppy})_2] \cdot 7\text{H}_2\text{O}$ [12] and Mn-based 1,3,5-benzenetricarboxylate [13], which have demonstrated outstanding electrochemical performance. Xu et al. synthesize a heterometallic (Ni, Co) 2,2'-bipyridine-5,5'-dicarboxylic coordination compound using a one-pot solvothermal approach, displaying a specific discharge/charge capacity of $0.65/0.64 \text{ mAh cm}^{-2}$ after 150 cycles at 0.1 mA cm^{-1} for LIBs [14]. Nonetheless, MCCs are facing challenges from the structural breakdown or pulverization phenomena resulting from the redox reaction of functional groups and metal cations, leading to high irreversible capacities and quick capacity decay.

To obtain MCCs with stable structures and high redox reaction activity, it is required to introduce suitable rigid structural units into organic ligand molecules for appropriate structures. Phosphonic acid with three oxygen atoms has a stronger coordination ability than carboxylic acid ligands with two oxygen atoms. As phosphonic acid is easily coordinated with metal ions to create P-O-M (M = metal ions) bonds and P-C bonds, the resulting phosphonic acid-based MCCs have stable structures and tunable voids [15].

Therefore, using low-cost phenyl phosphonic acid (PP) as the organic ligand and nickel tetrahydrate as a metal source, the different morphologies of nickel-based organic coordination compounds (Ni-PP- x , $x = 1, 2$, or 3) were synthesized via a one-pot microwave-assistant solvothermal method. Ni-PP- x morphologies were tuned by three typical reaction solvents (MeOH, DMF/EtOH/DI, and EtOH/DI), while comparing their physical and chemical properties, especially electrochemical performance. Besides, the lithium storage mechanism is investigated by *ex situ* X-ray photoelectron spectroscopy (XPS) and *ex situ* Fourier transform infrared spectroscopy (FT-IR).

2. Experimental

2.1. Chemicals

All the mentioned chemicals were used as purchased without further purifications, including nickel acetate tetrahydrate ($\text{Ni}(\text{CH}_3\text{COO})_2 \cdot 4\text{H}_2\text{O}$, 98%, Adamas Reagent Co., Ltd., Shanghai, China), phenylphosphonic acid (PP, 98%, Adamas Reagent Co., Ltd., Shanghai, China), N, N-dimethylformamide (DMF, 99.8%, Adamas Reagent Co., Ltd., Shanghai, China), methanol (MeOH, 99%, Sinopharm Chemical Reagent Co., Ltd., Shanghai, China), ethanol (EtOH, 99%, Sinopharm Chemical Reagent Co., Ltd., Shanghai, China), acetylene black (ACET, Battery grade, Xianfeng Nanomaterial Technology Co., Ltd., Nanjing, China), polyethylene difluoride (PVDF, Battery grade, Xianfeng Nanomaterial Technology Co., Ltd., Nanjing, China), 1-Methyl-2-Pyrrolidone (NMP, 98%, Sinopharm Chemical Reagent Co., Ltd., Shanghai, China), lithium tablet (Li, Battery grade, Zhongneng Lithium Co., Ltd., Tianjin, China), and LiPF_6 /(ethylene carbonate + diethyl carbonate electrolyte (1 M LiPF_6 , EC: DEC = 1: 1 (v/v), battery grade, Duoduo Reagent Network).

2.2. Synthesis of Ni-PP-x Products

Ni-PP-x ($x = 1, 2,$ or 3) samples were synthesized using a microwave-assisted solvothermal technique. Initially, $\text{Ni}(\text{CH}_3\text{COO})_2 \cdot 4\text{H}_2\text{O}$ (0.3 mmol) was dissolved in MeOH (9 mL) solvent, followed by strong stirring for 0.5 h as solution A. MeOH (6 mL) solvent was combined with PP (0.5 mmol) and constant stirred for 0.5 h as solution B. Following that, solution B was gradually added to solution A while stirring for 20 min. The final solution was put into a special glass bottle and stored in a microwave apparatus for 2 h at 100°C . After cooling to ambient temperature and repeatedly washing with MeOH, a kind of green precipitate was gathered and dried at 80°C , marked as Ni-PP-1 material. Similarly, Ni-PP-2 and Ni-PP-3 were synthesized by the identical procedure, except that the solvents of Ni-PP-2 and Ni-PP-3 were changed to DMF/EtOH/deionized water (DI) and EtOH/DI, respectively.

2.3. Material Characterizations

Scanning electron microscopy (SEM, JSM-6700F) and transmission electron microscopy (TEM, JEM-2010F) were applied to study the morphologies of the Ni-PP-x. The structural information was obtained using an X-ray diffractometer (XRD, Rigaku D/max-2550V, Cu $K\alpha$ radiation, 5°min^{-1}), and the measured data were identified through a PDF-2 (2021) database. Fourier transform infrared spectroscopy (FTIR, BIO-RADFTS 135) was used to characterize the information about the molecular structure. The element contained on the surface and the content and valence state of the element in the materials were assessed using X-ray photoelectron spectroscopy (XPS, Thermo Scientific K-Alpha). A micromeritics ASAP 2460 apparatus was used to measure the porous structures and surface area based on the N_2 adsorption-desorption isotherms. Simultaneous thermal analysis (TG-DSCA, Hitachi TGA 8000) was used to investigate the decomposition mode of materials, content of organic matter and inorganic matter in materials. The test was carried out under N_2 atmosphere and $20^\circ\text{C min}^{-1}$ at room temperature to 800°C .

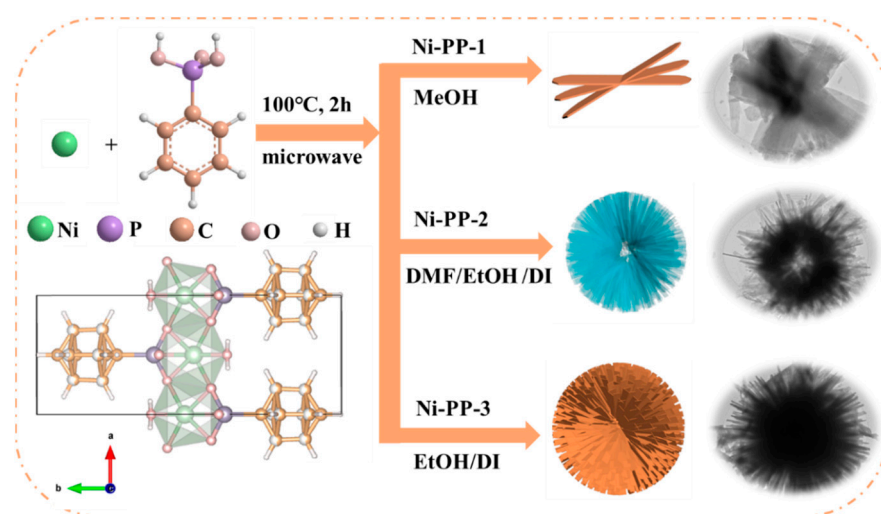
2.4. Electrochemical Measurements

The anode paste was mixed with active material, ACET, and PVDF (6: 3: 1, $w/w/w$), and coated on copper foil with a mass load of $\sim 1.5 \text{ mg cm}^{-2}$. The CR2032 cells were fabricated utilizing a reference electrode (lithium foil), separator (polypropylene film (Celgard 2400)), and electrolyte (1 M LiPF_6 , EC: DEC = 1: 1 (v/v)). The charge-specific capacity of the battery can be obtained by a constant current mode of charge/discharge tests, which were measured by LAND-CT2001. The galvanostatic intermittent titration technique (GITT) was also measured by LAND-CT2001 with a current pulse of 0.1 A g^{-1} for 5 min in a voltage range from 0.01 to 3.0 V, followed by a relaxation interval of 15 min. The reaction mechanism, reversible degree, and polarization degree of the battery were analyzed by cyclic voltammetry (CV) results, which were collected on an electrochemical workstation (CHI 660D) at various sweep rates (0.1, 0.2, 0.4, 0.6, and 0.8 mV s^{-1}). The reaction resistances of the charge transfer process were obtained by electrochemical impedance spectroscopy (EIS), which was carried out on an electrochemical workstation (Autolab PGDTAT101) between 0.01 and 10^5 Hz .

3. Results and Discussion

The synthesis process and molecular structure of Ni-PP-x ($x = 1, 2,$ or 3) materials are depicted in Scheme 1. With the $\text{Ni}(\text{CH}_3\text{COO})_2 \cdot 4\text{H}_2\text{O}$ as the nickel source and PP as the ligand, three materials with different morphologies were prepared using a one-step microwave-assistant solvothermal method with varying solvent types. In addition, the crystal structure of Ni-PP-x ($x = 1, 2,$ or 3) is composed of one Ni^{2+} , three PPs, and one coordination H_2O , where the Ni^{2+} is coupled to the oxygen atom of the phosphonate ligand and the oxygen atom of the water molecule. The morphology and internal structure of the three samples, illustrated by SEM and TEM images, are shown in Figure 1. Ni-PP-1 material with a disordered stacking structure composed of thin micro sheets was

obtained, when MeOH was utilized as the solvent (Figure 1a,d). When the solvent was switched to DMF/DI/EtOH, hollow urchin-like microspheres, made of many nanosheets with different diameters, were produced and marked as Ni-PP-2 with an average size of $\sim 2.3 \mu\text{m}$ (Figure 1b,e). When the solvent is changed to the DI/EtOH mixture, Ni-PP-3 material is achieved with an urchin-like microsphere morphology but is composed in a thicker nanosheet, showing a larger spherical size ($\sim 6.5 \mu\text{m}$) and a solid structure (Figure 1c,f). It is further determined that the morphology and structure of Ni-PP- x ($x = 1, 2, \text{ or } 3$) crystals are significantly influenced by the reaction solvents throughout the crystal formation process, implying that DMF is vital to creating hollow and urchin-like structures by chemical etching. Among them, Ni-PP-2, with its special structure, offers an interconnected conductive network that facilitates electrolyte penetration, ion migration, and easing volume variations. Besides, the element mapping images of Ni-PP-2 are shown in Figure 1g–k, indicating the homogenous elemental distribution of C, O, P, and Ni.



Scheme 1. The synthesis process and molecular structure diagram of Ni-PP- x ($x = 1, 2, \text{ or } 3$) were obtained in varying solvents.

Figure 2a shows the X-ray diffraction (XRD) patterns of Ni-PP- x ($x = 1, 2, 3$), and all the characteristic peaks are well indexed to the Ni-PP ($\text{Ni}(\text{O}_3\text{PC}_6\text{H}_5)\cdot\text{H}_2\text{O}$, orthorhombic, Pmn2/1) standard card (PDF # 00-049-2391), suggesting that all the samples have comparable molecules and crystal structures [16]. Four strong peaks at 6.1° , 12.3° , 17.1° , and 19.4° correspond to the (010), (020), (110), and (011) lattice planes, respectively. As shown in Figure 2b, the FTIR peaks at about 3464 cm^{-1} is the characteristic peak of the -OH stretching vibrations, proving the presence of free water molecules in the Ni-PP- x ($x = 1, 2, \text{ or } 3$) samples. Other peaks at about 3052 , $1618/1486$, 1400 , $1093/975$, and 582 cm^{-1} are responsible for the vibration of C-H, C=C, C-P, P-O-Ni, and Ni-O bonds, respectively [17–19]. Besides, stronger P-O-Ni and Ni-O characteristic infrared peaks are observed in Ni-PP- x ($x = 1, 2, \text{ or } 3$) than in PP, which suggests that Ni^{2+} is successfully coordinated with PP. Besides, the peaks of Ni 2p, O 1s, C 1s, and P 2p are displayed in the full XPS spectrum of the material (Figure S1), confirming the presence of the aforementioned elements. Through the analysis of curve-fitted Ni 2p spectra in Figure 2c, a pair of peaks at 854.92 and 856.05 eV are attributed to Ni^{2+} and Ni^{3+} in Ni 2p $_{3/2}$, the peak at 872.94 eV corresponds to Ni 2p $_{1/2}$ and peaks at 861.07 and 878.94 eV are associated with satellite signals [20,21]. That is further evidence that the central metal ion in Ni-PP-2 exists as Ni^{2+} since the spin energy difference between Ni 2p $_{1/2}$ and Ni 2p $_{3/2}$ is 17.9 eV . In the high-resolution spectra of C 1s, the peaks at 284.3 and 284.8 eV are mostly derived from C=C and C-C bonds (Figure 2d) [22]. In Figure 2e, the peak at 132.7 eV is related to P^{5+} in the phosphonic acid group [23]. Moreover, the peaks of the O 1s spectra at 530.9 and 532.7 eV are assigned to Ni-O-P and H-O-H (Figure 2f) [24,25]. The conclusion reached is that the Ni-PP-2 material was successfully

formed by the analyses indicated above. Additionally, according to IUPAC classification, N_2 adsorption/desorption curves of Ni-PP- x ($x = 1, 2$, or 3) all belong to the type III curve with H3 hysteresis loop (Figure S2), showing that they contain abundant mesoporous structure [26,27]. In comparison to Ni-PP-1 ($34.6 \text{ m}^2 \text{ g}^{-1}$ and 19.0 nm) and Ni-PP-3 ($33.2 \text{ m}^2 \text{ g}^{-1}$ and 14.7 nm), Ni-PP-2 has a greater specific surface area and pore size ($47.7 \text{ m}^2 \text{ g}^{-1}$ and 24.1 nm). This structure of Ni-PP-2 provides rich and stable channels for Li^+ migration in the battery and is helpful in promoting full electrolyte diffusion, facilitating the reduction of concentration polarization. As shown in Figure S3, simultaneous thermal analysis (TG-DSC) was performed to test the thermal stability of Ni-PP-2. It is seen that the curves between room temperature and $283 \text{ }^\circ\text{C}$ have a lowered portion (8.5%), which is caused by the release of synergistic water molecules. The sharply declining portion (38.5%) in the $283\text{--}613 \text{ }^\circ\text{C}$ range is attributed to the degradation of organic ligands. As a result, Ni-PP-2 has better thermal stability because of the existence of the C-P bond [28].

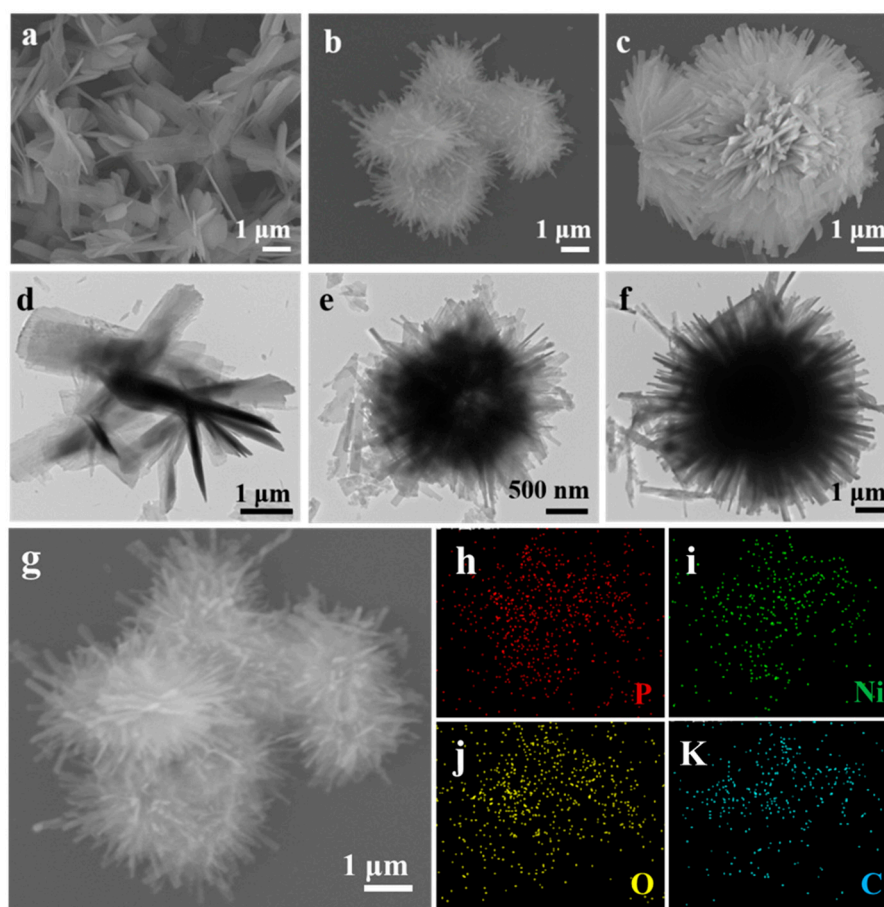


Figure 1. SEM images of (a) Ni-PP-1, (b) Ni-PP-2, (c) Ni-PP-3, and TEM images of (d) Ni-PP-1, (e) Ni-PP-2, (f) Ni-PP-3, and elemental mapping images of Ni-PP-2 (g–k).

The electrochemical performances for Ni-PP- x ($x = 1, 2$, or 3) were investigated between 0.01 and 3.0 V and illustrated in Figure 3. As shown in Figure 3a, their initial rechargeable capacities at 0.2 A g^{-1} are 743 mAh g^{-1} for Ni-PP-1, 964 mAh g^{-1} for Ni-PP-2, and 757 mAh g^{-1} for Ni-PP-3, with coulombic efficiency (CE) values of 46.9%, 52.6%, and 43.4%, respectively. It is hypothesized that more Li^+ may be absorbed in Ni-PP-2 due to its hollow and urchin-like structure, providing more active sites and high ionic conductivity. Among them, steadily increasing CEs ($\sim 98\%$) in the later cycles of Ni-PP-2 are primarily obtained, resulting in more ions and chemical bonds taking part in the in-depth redox reactions. Encouragingly, the reversible capacity of Ni-PP-2 is still 1193 mAh g^{-1} after 200 cycles, which is significantly higher than that of Ni-PP-1 (436 mAh g^{-1}) and Ni-PP-3

(617 mAh g⁻¹). When the current density is raised to 1.0 A g⁻¹, Ni-PP-1, Ni-PP-2, and Ni-PP-3 display their rechargeable capacities of 688, 1175, and 707 mA h g⁻¹ after 600 cycles, respectively (Figure S4). Notably, the Ni-PP-2 material exhibits the highest long cycling ability, providing a high Li-storage capacity of 713 mAh g⁻¹ after 800 cycles at 2.0 A g⁻¹, which is higher than those of Ni-PP-1 (517 mAh g⁻¹) and Ni-PP-3 (529 mAh g⁻¹), as presented in Figure 3b. The excellent cycling performance of Ni-PP-2 is primarily associated with its distinctive hollow and urchin-like structure, high specific surface area, and large mesopores, which aid in improving structural stability by alleviating volume variations and reducing concentration polarization during cycles. There is an abnormal phenomenon in the cycling performance of Ni-PP-x (x = 1, 2, or 3) under various current densities undergoing a process of capacity dropping in the first few cycles and capacity increasing, in the following cycles, which may be related to electrode activation, particle refining, surface area increasing and mechanical deterioration [29–31]. According to Table S1, Ni-PP-2 has demonstrated competitive electrochemical performance when compared to other similar coordination compounds in the literature [15,18,32–36]. Figure 3c displays the CV curves of the first three scan cycles for Ni-PP-2 in the voltage range of 0.01–3.0 V at 0.1 mV s⁻¹. According to previous reports [37], the irreversible and broad peak at 0.91 V in the initial negative sweep is associated with the production of solid electrolyte interphase (SEI). The small reduction peaks at 1.64 and 1.41 V could be attributed to the Li⁺ intercalation in organic ligands, and the reduction peak at 0.69 V is due to the conversion process of Ni²⁺ to Ni⁰ and reactions between Li⁺ cations and benzene rings. During the first positive CV sweep, the peak at 1.23 V is a result of the delithiation reaction between Li⁺ and C=C bond, whereas the peak at 0.81 V is caused by the oxidation of Ni⁰ to Ni²⁺. In subsequent cycles, no other visible redox reaction peak is observed, proving the stable reaction behaviors of Ni-PP-2 material during the cycling process. Furthermore, the second and third CV curves are almost in line with one another, which is consistent with the reaction voltage platforms at 0.2 A g⁻¹ (Figure 3d), demonstrating that the lithiation/delithiation behaviors of Li⁺ of Ni-PP-2 electrode are tending to be stable and more reversible in the succeeding cycles. As depicted in Figure S5, there is a slight discrepancy in the first charge/discharge curve of Ni-PP-2 at 0.2 A g⁻¹ and 2.0 A g⁻¹ due to the quick extraction and insertion of Li⁺ produced by the rise in current density. However, the shapes of the charge/discharge curves remained consistent over all subsequent cycles, and the cycling capacity gradually increased with the weakening of the polarization phenomenon and electrode activation. Moreover, the rate performances of Ni-PP-x (x = 1, 2, or 3) at stepwise current densities of 0.1, 0.2, 0.5, 1.0, and 2.0 A g⁻¹ are explored in Figure 3e. With reversible capacities of 540, 481 and 378, 316, and 239 mA h g⁻¹ at above current densities, the Ni-PP-2 electrode outperforms other materials in terms of rate property. Due to the special coordination structure, the capacity of the Ni-PP-2 electrode still reaches up to 793 mAh g⁻¹ even when the current density is reduced to 0.1 A g⁻¹. In Figure S6, the charge/discharge curves of the well-defined Ni-PP-x were well maintained, demonstrating their remarkable electrochemical stability at varying current densities.

Further analyzing the lithium-storage mechanism of Ni-PP-2 during cycling, the ex situ XPS analysis technologies are carried out, as displayed in Figure 4a,b. The peaks at 284.3 and 284.8 eV in the C 1s spectra of pristine conditions are assigned to the C=C and C-C bonds, as prepared in Figure 4a. The strength of the C=C peak gradually reduced as Ni-PP-2 was discharged to 0.01 V, whereas the intensity of the C-C peak gradually increased, implying the lithiation of the benzene ring. Moreover, the peaks at 284.3 and 284.8 eV were indexed to the Li₂CO₃ and C-O bonds, respectively, which clearly illustrated the reaction of SEI film formation [38]. The peak intensities of C-C and C=C changed inversely when charged to 3.0 V, but they did not revert to their initial states, which may be related to the happening of partially reversible reactions and the irreversible growth of SEI film. The peaks at 856.1 and 874.0 eV are related to Ni 2p_{3/2} and Ni 2p_{1/2} in the high-resolution spectra of Ni 2p in pristine conditions (Figure 4b). The bonding energy of the two distinctive peaks decreases when it is fully discharged to 0.01 V, showing that Ni²⁺

is reduced to metal Ni⁰ and subsequently recovered after charging, proving that Ni-PP-2 could store Li⁺ reversibly in the Ni²⁺ center via the conversion reaction mechanism [39]. The lithium storage mechanism of the Ni-PP-2 electrode was further confirmed by the ex situ FTIR spectra at varied voltages, as shown in Figure 4c. After complete discharge, the intensities of the C=C peak (1618 cm⁻¹) and the Ni-O-P peaks (1093 and 975 cm⁻¹) are decreased, which are attributed to the intercalation of Li⁺ in the benzene ring and the reduction of Ni²⁺ to Ni⁰, respectively. When charged to 3.0 V, the intensities of the two peaks increased but did not entirely recover, indicating the partially reversible Li⁺ extraction from the benzene ring and the partial oxidation of Ni⁰ to Ni²⁺, as well as the formation of an irreversible SEI film. These phenomena are in line with the CV curves and the voltage platforms in the first cycle. Owing to the aforementioned analysis results, the corresponding electrochemical mechanism of Ni-PP-2 is proposed, as illustrated in Figure 4d. The Ni-PP compound is recognized as the redox reactions of a benzene ring and O-Ni²⁺/O-Ni⁰ coordination bonds with Li⁺ cations, showing 6Li⁺ can be reversibly inserted and removed from each benzene ring in the organic ligand and 2Li⁺ can be absorbed via the reversible conversion reaction between Ni²⁺ and Ni⁰. Therefore, it exhibits rapid reaction kinetics and high active site consumption, leading to high rate ability and great cycle stability.

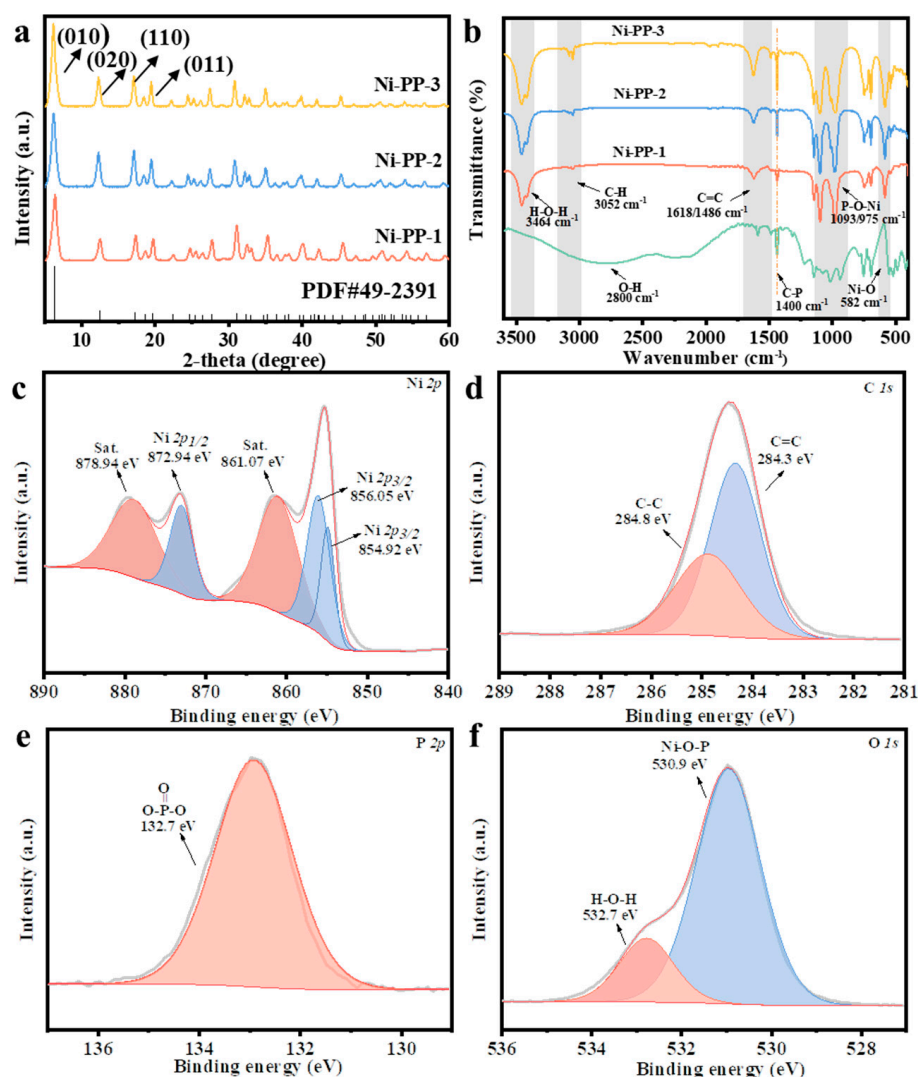


Figure 2. The material characterizations of Ni-PP-*x* (*x* = 1, 2, 3): (a) XRD patterns, (b) FTIR spectra of Ni-PP-*x* (*x* = 1, 2, 3) and PP, and XPS spectra of Ni-PP-2: (c) Ni 2p, (d) C 1s, (e) P 2p, and (f) O 1s.

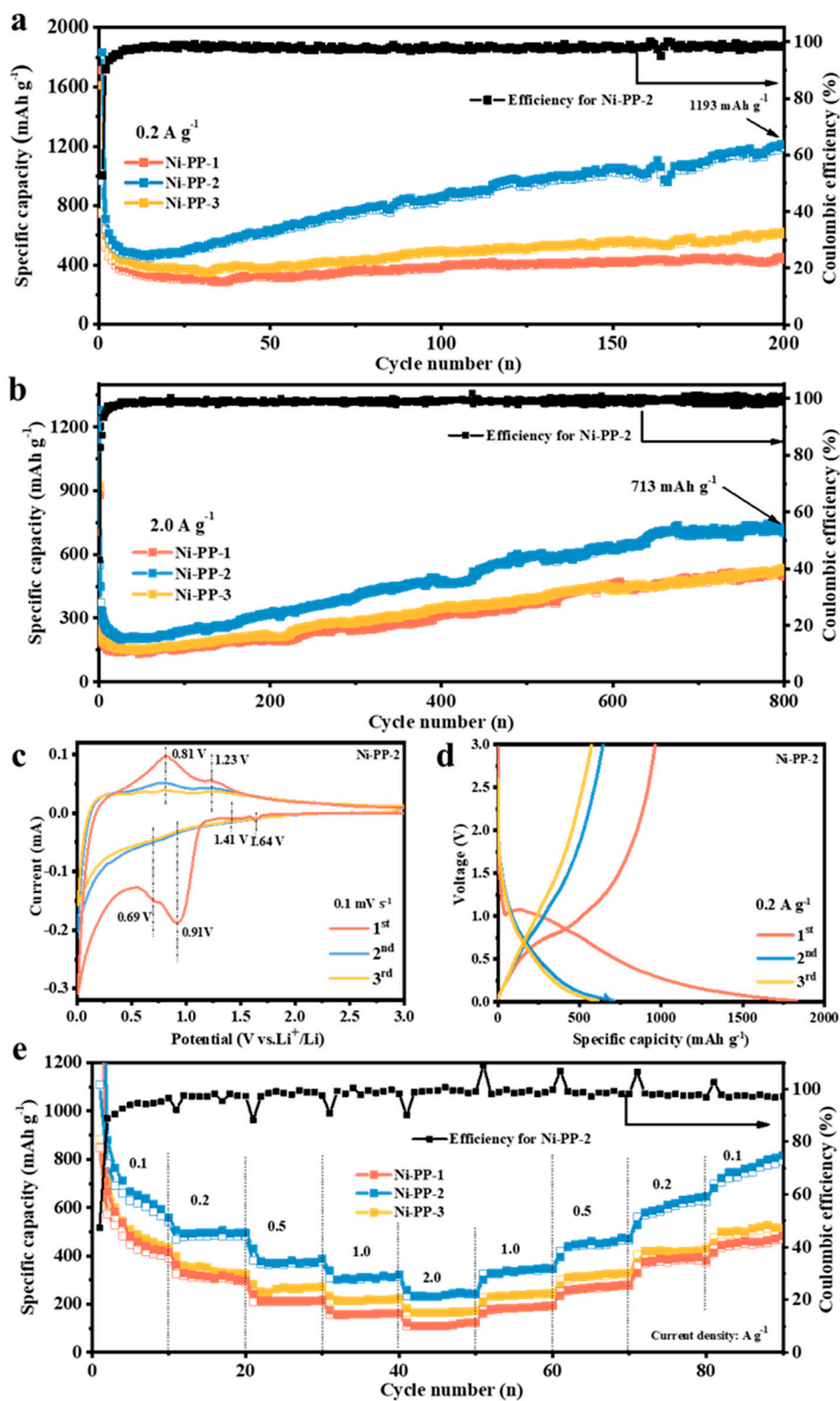


Figure 3. Cycling performances of Ni-PP-*x* (*x* = 1, 2, or 3) electrodes at (a) 0.2 A g⁻¹ and (b) 2.0 A g⁻¹, (c) The first three CV curves at 0.1 mV s⁻¹ of Ni-PP-2, (d) the first three charge/discharge curves at 0.2 A g⁻¹ of Ni-PP-2, and (e) rate performance of Ni-PP-*x* (*x* = 1, 2, or 3).

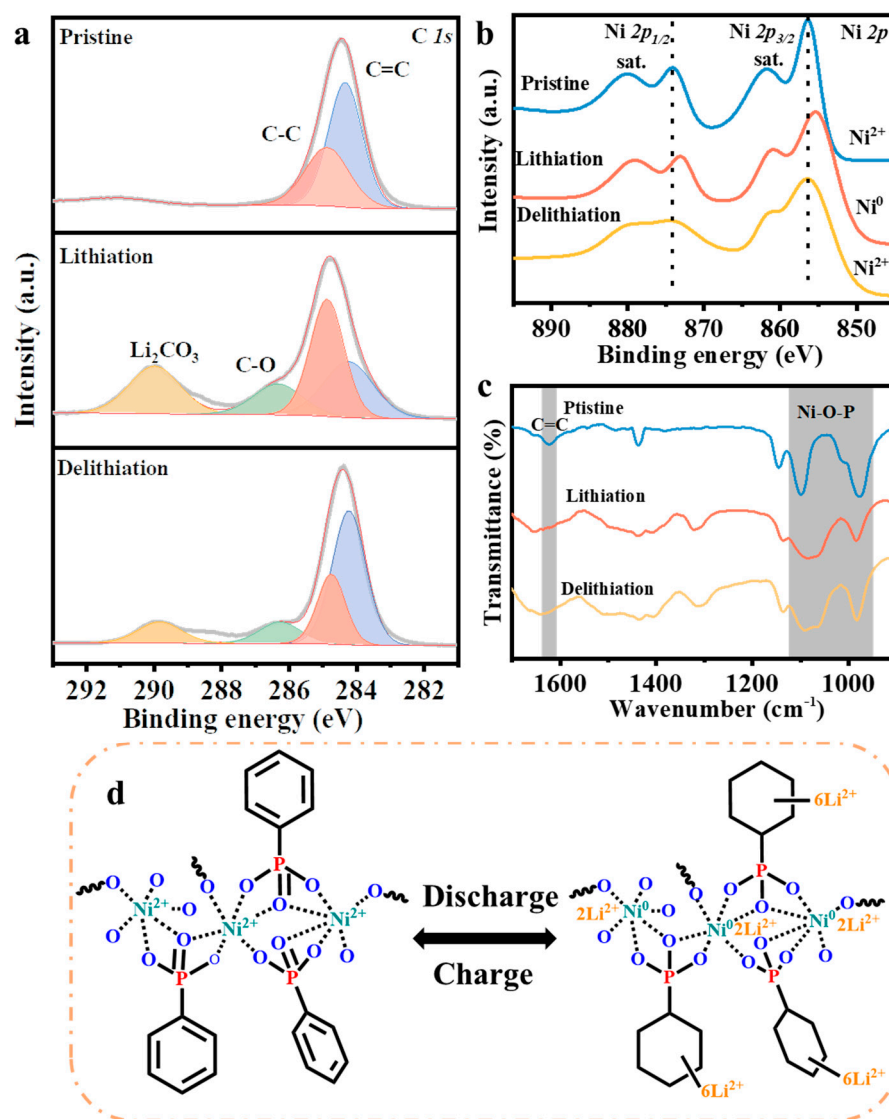


Figure 4. Ex situ XPS spectra of (a) C 1s and (b) Ni 2p for Ni-PP-2 during lithiation/delithiation processes, (c) ex situ FTIR spectra for Ni-PP-2 during lithiation/delithiation processes, and (d) the proposed lithiation/delithiation reaction mechanism diagram of Ni-PP-2.

To analyze the reason for the excellent electrochemical performance of Ni-PP-2, further reaction kinetics were examined through CV curves, as depicted in Figure 5a. The CV curves at 0.1, 0.2, 0.4, 0.6, and 0.8 mV s⁻¹ have shown similar profiles, indicating good reaction reversibility. The lithium storage kinetics of the Ni-PP-2 electrode were further analyzed by the following formula [40,41]:

$$i = av^b \quad (1)$$

$$\log(i) = b^* \log(v) + \log(a) \quad (2)$$

where i and v represent the peak current and sweep rate, respectively, while a and b serve as constants. The b value established by the slope of the $\log(v)$ versus $\log(i)$ curve is directly reflecting the types of reaction behavior. The electrode is mainly displaying a diffusion process when the b value is approaching 0.5, and a pseudo-capacitive behavior predominates when it is close to 1.0 [42,43]. The b -values of the Ni-PP-2 electrode are 0.74 in the cathodic peak and 0.93 in the anodic peak, as shown in Figure 5b, revealing that pseudo-capacitive behavior dominates the electrochemical process. The specific capacity contribution of pseudocapacitance can be calculated using the following formula [44]:

$$i(v) = k_1v + k_2v^{1/2} \quad (3)$$

where k_1v and $k_2v^{1/2}$ represent the capacity contributions from pseudo-capacitance control and diffusion control, respectively. Moreover, k_1 and k_2 are the slope and intercept of the linear relationship between $i/v^{1/2}$ and $v^{1/2}$, respectively. It is calculated that the pseudo-capacitive contribution of Ni-PP-2 accounts for about 72.9% at 0.6 mV s^{-1} (Figure 5c). According to the same methodology, all of the pseudo-capacitive contributions at different scan rates are calculated and displayed in Figure 5d, which shows a high pseudo-capacitive contribution of 73.3% at 0.8 mV s^{-1} . Thus, the high rate performance of Ni-PP-2 stems from its excellent kinetic behavior via its pseudo-capacitive contribution [45,46].

The electrochemical resistances of Ni-PP- x ($x = 1, 2, \text{ or } 3$) materials are displayed in Figure 5e, examined at the open-circuit voltage and after 100 cycles at 0.1 A g^{-1} . After fitting them based on the equivalent circuit in Figure 5e, specific values of electrolyte resistance (R_s , R_1), charge transfer resistance (R_{ct} , R_2), capacitance (CPE), and Warburg impedance were obtained, as shown in Table S2, demonstrating the Wo-P values of Ni-PP- x are all close to 0.5 in the pristine state, while the value of Ni-PP-2 is much closer to 0.5 than those of Ni-PP-1 and Ni-PP-3 after 100 cycles. [47,48]. The values of R_{ct} for Ni-PP-2, Ni-PP-1, and Ni-PP-3 electrodes at the open circuit voltage are about 151.6, 224.0, and 213.7 Ω , respectively. The semicircle diameters of the three materials dramatically shrank after 100 cycles, and the R_{ct} values of Ni-PP-2, Ni-PP-1, and Ni-PP-3 are about 99.5, 142.8, and 123.0 Ω , respectively, suggesting that the electrochemical resistance of Ni-PP-2 is the smallest and the charge transfer resistances of them are slightly decreased after many cycles. This might be one of the reasons for the phenomenon of capacity decreasing in the first few cycles and increasing after many cycles. Moreover, the Ni-PP-2 electrode has exhibited the lowest charge transfer resistance and diffusion resistance, indicating that it has displayed a higher electrical conductivity and rapid ionic mobility and hence achieved outstanding cycling and rate performances.

Moreover, the Li^+ diffusion coefficients of Ni-PP- x ($x = 1, 2, \text{ or } 3$), reflecting the ionic mobility, are affirmed by the galvanostatic intermittent titration technique (GITT) method. Figure S7 displays the three continuous GITT curves at 0.1 A g^{-1} , with charging and discharging interval times of 5 min. The diffusion coefficient can be calculated using Fick's second law [49]:

$$D_{\text{Li}^+} = \frac{4}{\pi\tau} \left(\frac{m_B V_M}{M_B S} \right)^2 \left(\frac{\Delta E_s}{\Delta E_t} \right)^2 \left(\tau \ll \frac{L^2}{D_{\text{Li}^+}} \right) \quad (4)$$

where τ is the constant current titration time, V_M is the molar volume of the active material, m_B , and M_B are the weight and molecular weight of the active material, S is the total contact area between the electrolyte and the electrode, ΔE_s and ΔE_t are the steady-state voltage changes during constant current titration, and L is the diffusion length. The diffusion coefficients calculated using the formula are displayed in Figure 5f based on the GITT reaction process and the linear relationship between E and $\tau^{1/2}$ in Figure S8, displaying that Ni-PP-2 has the highest values of $\sim 1.91 \times 10^{-13} \text{ cm}^2 \text{ s}^{-1}$, which is greater than those of Ni-PP-1 ($\sim 0.95 \times 10^{-13} \text{ cm}^2 \text{ s}^{-1}$) and Ni-PP-3 ($\sim 1.40 \times 10^{-13} \text{ cm}^2 \text{ s}^{-1}$). That is highly ascribed to the rapid Li^+ mobility in the Ni-PP-2 electrode, the special hollow and urchin-like microspheres, and the superior mechanical stability to inhibit volume variations.

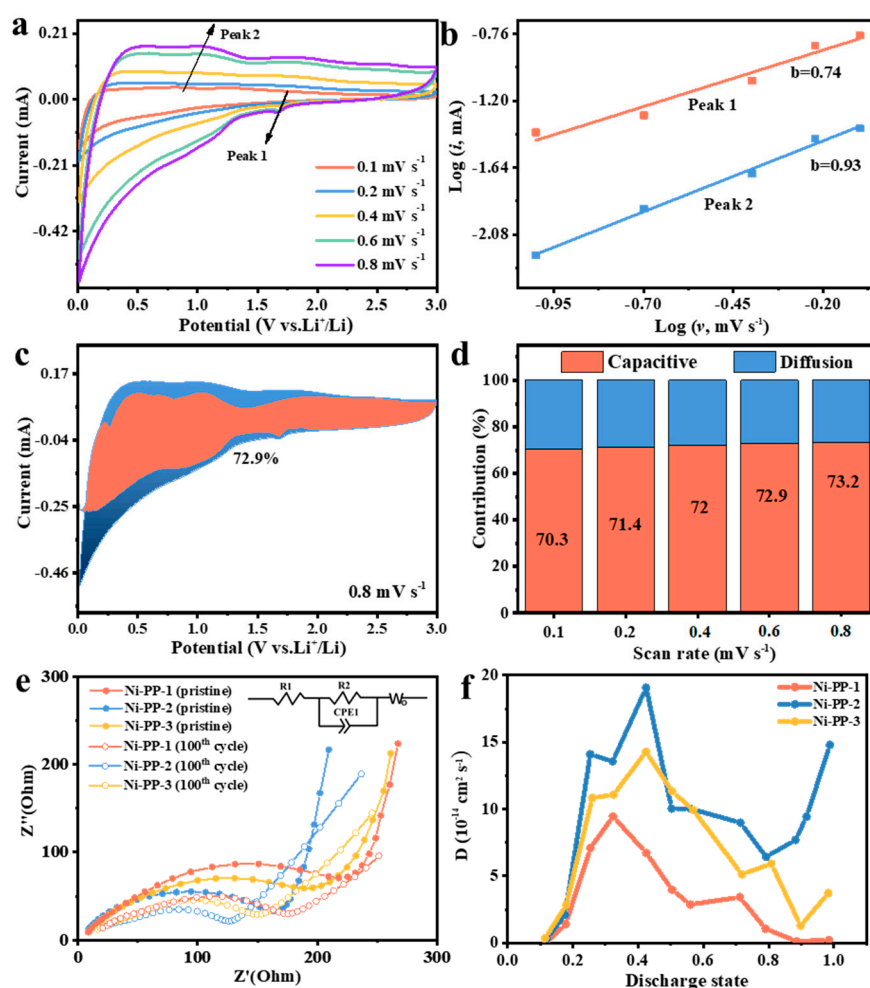


Figure 5. Kinetic analysis of the Ni-PP-2 electrode: (a) CV curves at different scan rates from 0.1 to 0.8 mV s^{-1} , (b) the relationship between $\log(i)$ and $\log(v)$, (c) the ratio of diffusion (blue area) and pseudo-capacitive (orange area) at 0.6 mV s^{-1} , and (d) the contribution ratio of diffusion vs. pseudo-capacitive under different scanning rates. (e) Nyquist plots of the uncirculated and after 100 cycles at 0.1 A g^{-1} . (f) The calculated Li^+ chemical diffusion coefficients are based on GITT.

4. Conclusions

Nickel-based coordination compounds (Ni-PP- x , $x = 1, 2$, or 3) were synthesized with tunable morphologies by altering the solvent composition by an efficient microwave irradiation solvothermal method. When used as the anode for LIBs, the Ni-PP-2 electrode with a hollow and urchin-like structure showed the longest cycle lives and maintained the highest capacity of 713 mAh g^{-1} at 2.0 A g^{-1} after 800 cycles, indicating the superior electrochemical performance of the Ni-PP-2 electrode is associated with the intrinsic features of the large surface area, the shortest ionic transportation paths, and the highest ionic diffusion coefficient. Moreover, the reaction mechanism of the Ni-PP-2 electrode was confirmed as the redox reactions between Li^+ cations and the benzene ring and $\text{O-Ni}^{2+}/\text{O-Ni}^0$ coordination bonds by many sophisticated techniques of ex situ XPS, ex situ FTIR, and CV curves, and the lithium behavior was confirmed as the pseudo-capacitive-dominated way. Therefore, this work has opened a new avenue for applying metal coordination compounds as electrodes for LIBs, and the corresponding reaction mechanism is proposed, shining light on the application of MCC compounds as electrodes for LIBs and other energy storage systems.

Supplementary Materials: The following supporting information can be downloaded at: <https://www.mdpi.com/article/10.3390/batteries9060313/s1>, Figure S1: The survey spectrum of Ni-PP-2; Figure S2: N₂ adsorption-desorption isotherms and pore size distribution of (a) Ni-PP-1, (b) Ni-PP-2, and (c) Ni-PP-3; Figure S3: TG-DSC curves of Ni-PP-2; Figure S4: Cycling performances of Ni-PP-x (x = 1, 2, 3) at 1.0 A g⁻¹; Figure S5: Charge/discharge curves of Ni-PP-2 at different cycles under (a) 0.2 A g⁻¹, and (b) 2.0 A g⁻¹; Figure S6: Charge/discharge curves at different current densities: of (a) Ni-PP-1, (b) Ni-PP-2, and (c) Ni-PP-3; Figure S7: Initial discharge GITT curves of (a) Ni-PP-1, (b) Ni-PP-2, and (c) Ni-PP-3; Figure S8: One single GITT profile of Ni-PP in the discharge process of (a) Ni-PP-1, (b) Ni-PP-2, and (c) Ni-PP-3. The corresponding linear relationship for the E versus $\tau^{1/2}$ in the discharge process of (d) Ni-PP-1, (e) Ni-PP-2, and (f) Ni-PP-3; Table S1: Electrochemical performance of coordination compounds as anodes for LIBs. (RRC: retained reversible capacity, CD: current density); Table S2: Fitting results of electrochemical impedance spectrum [15,18,32–36].

Author Contributions: Conceptualization, Y.L., L.W. (Lei Wang), Z.L. and S.C.; validation, L.W. (Leilei Wang) and Y.Z. investigation, Y.L., L.W. (Lei Wang) and Z.L.; resources, W.S., L.L., Y.W. and S.C.; data curation, Y.L., L.W. (Lei Wang) and Z.L.; writing—original draft preparation, Y.L. and L.W.; writing—review and editing, L.W. (Lei Wang) and S.C.; project administration, S.C. All authors have read and agreed to the published version of the manuscript.

Funding: This research received no external funding.

Data Availability Statement: Data are available from the corresponding author on reasonable request.

Acknowledgments: The authors gratefully acknowledge the National Natural Science Foundation of China (21975154, 22179078), Shanghai Municipal Education Commission (Innovation Program: 2019-01-07-00-09-E00021), and the Innovative Research Team of High-level Local Universities in Shanghai. The authors thank the Laboratory for Microstructures, Instrumental Analysis, and Research Center of Shanghai University for offering access to material characterizations.

Conflicts of Interest: The authors declare no conflict of interest. The funders had no role in the design of the study; in the collection, analyses, or interpretation of data; in the writing of the manuscript, or in the decision to publish the results.

References

1. Wang, E.; Xiao, D.; Wu, T.; Wang, B.; Wang, Y.; Wu, L.; Zhang, X.; Yu, H. Stabilizing oxygen by high-valence element doping for high-performance Li-rich layered oxides. *Battery Energy* **2023**, *2*, 20220030. [[CrossRef](#)]
2. Cui, X.; Chen, J.; Sun, Z.; Wang, L.; Peng, Q.; Xiao, B.; Zhao, L.; Zheng, H.; Wang, Y.; Wang, J.; et al. A General Route for Encapsulating Monodispersed Transition Metal Phosphides into Carbon Multi-Chambers toward High-Efficient Lithium-Ion Storage with Underlying Mechanism Exploration. *Adv. Funct. Mater.* **2023**, *33*, 2212100. [[CrossRef](#)]
3. Azam, M.A.; Safie, N.E.; Ahmad, A.S.; Yuza, N.A.; Zulkifli, N.S.A. Recent advances of silicon, carbon composites and tin oxide as new anode materials for lithium-ion battery: A comprehensive review. *J. Energy Storage* **2021**, *33*, 102096. [[CrossRef](#)]
4. Paul, S.; Rahman, M.A.; Islam, M.S.; Islam, M.R.; Siddiqui, S.E.T. Nanostructured anatase TiO₂ as anode of high-performance lithium-ion batteries. *Battery Energy* **2022**, *1*, 20220018. [[CrossRef](#)]
5. Tian, W.; Sun, H.; Chen, L.; Wangyang, P.; Chen, X.; Xiong, J.; Li, L. Low-dimensional nanomaterial/Si heterostructure-based photodetectors. *InfoMat* **2019**, *1*, 140–161. [[CrossRef](#)]
6. Chen, Z.; Chen, Z.; Farha, O.K.; Chapman, K.W. Mechanistic insights into nanoparticle formation from bimetallic metal-organic frameworks. *J. Am. Chem. Soc.* **2021**, *143*, 8976–8980. [[CrossRef](#)]
7. Jiang, Q.; Xiong, P.; Liu, J.; Xie, Z.; Wang, Q.; Yang, X.Q.; Hu, E.; Cao, Y.; Sun, J.; Xu, Y.; et al. A redox-active 2D metal-organic framework for efficient lithium storage with extraordinary high capacity. *Angew. Chem. Int. Ed.* **2020**, *59*, 5273–5277. [[CrossRef](#)]
8. Li, C.; Hu, X.; Tong, W.; Yan, W.; Lou, X.; Shen, M.; Hu, B. Ultrathin manganese-based metal-organic framework nanosheets: Low-cost and energy-dense lithium storage anodes with the coexistence of metal and ligand redox activities. *ACS Appl. Mater. Interfaces* **2017**, *9*, 29829–29838. [[CrossRef](#)]
9. Hu, H.; Lou, X.; Li, C.; Hu, X.; Li, T.; Chen, Q.; Shen, M.; Hu, B. A thermally activated manganese 1,4-benzenedicarboxylate metal organic framework with high anodic capability for Li-ion batteries. *New J. Chem.* **2016**, *40*, 9746–9752. [[CrossRef](#)]
10. Li, X.; Cheng, F.; Zhang, S.; Chen, J. Shape-controlled synthesis and lithium-storage study of metal-organic frameworks Zn₄O(1,3,5-benzenetribenzoate)₂. *J. Power Sources* **2006**, *160*, 542–547. [[CrossRef](#)]
11. Saravanan, K.; Nagarathinam, M.; Balaya, P.; Vittal, J.J. Lithium storage in a metal organic framework with diamondoid topology—A case study on metal formates. *J. Mater. Chem.* **2010**, *20*, 8329–8335. [[CrossRef](#)]
12. Hu, L.; Lin, X.M.; Mo, J.T.; Lin, J.; Gan, H.L.; Yang, X.L.; Cai, Y.P. Lead-Based Metal-Organic Framework with Stable Lithium Anodic Performance. *Inorg. Chem.* **2017**, *56*, 4289–4295. [[CrossRef](#)]

13. Maiti, S.; Pramanik, A.; Manju, U.; Mahanty, S. Reversible Lithium Storage in Manganese 1,3,5-Benzenetricarboxylate Metal-Organic Framework with High Capacity and Rate Performance. *ACS Appl. Mater. Interfaces* **2015**, *7*, 16357–16363. [[CrossRef](#)]
14. Xu, N.; Han, Q.; Zhu, L.; Xie, L.; Xu, J.; Zhang, W.; Yang, X.; Cao, X. Design and Synthesis of Heterometallic Ni–Co Organic Frameworks as Anode Materials for High-Performance Lithium Storage. *J. Electrochem. Soc.* **2022**, *169*, 030526. [[CrossRef](#)]
15. Chakraborty, D.; Dam, T.; Modak, A.; Pant, K.K.; Chandra, B.K.; Majee, A.; Ghosh, A.; Bhaumik, A. A novel crystalline nanoporous iron phosphonate based metal-organic framework as an efficient anode material for lithium ion batteries. *New J. Chem.* **2021**, *45*, 15458–15468. [[CrossRef](#)]
16. Cheng, Y.; Guo, X.; Xue, Y.; Pang, H. Controllable synthesis of a flower-like superstructure of nickel metal-organic phosphate and its derivatives for supercapacitors. *Appl. Mater. Today* **2021**, *23*, 101048. [[CrossRef](#)]
17. Vasylyev, M.; Neumann, R. Preparation, characterization, and catalytic aerobic oxidation by a vanadium phosphonate mesoporous material constructed from a dendritic tetraphosphonate. *Chem. Mater.* **2006**, *18*, 2781–2783. [[CrossRef](#)]
18. Chang, H.-L.; Bai, Y.-W.; Song, X.-Y.; Duan, Y.-F.; Sun, P.-P.; Tian, B.; Shi, G.; You, H.; Gao, J.; Shi, F.-N. Hydrothermal synthesis, structural elucidation and electrochemical properties of three nickel and cobalt based phosphonates as anode materials for lithium ion batteries. *Electrochim. Acta* **2019**, *321*, 134647. [[CrossRef](#)]
19. Roland, A.; Fullenwarth, J.; Ledeuil, J.B.; Martinez, H.; Louvain, N.; Monconduit, L. How carbon coating or continuous carbon pitch matrix influence the silicon electrode/electrolyte interfaces and the performance in Li-ion batteries. *Battery Energy* **2022**, *1*, 20210009. [[CrossRef](#)]
20. Jamil, S.; Fasehullah, M.; Jabar, B.; Liu, P.; Aslam, M.K.; Zhang, Y.; Bao, S.; Xu, M. Significantly fastened redox kinetics in single crystal layered oxide cathode by gradient doping. *Nano Energy* **2022**, *94*, 106961. [[CrossRef](#)]
21. Jamil, S.; Wang, H.; Fasehullah, M.; Aslam, M.K.; Jabar, B.; Ud Din, M.A.; Zhang, Y.; Sun, W.; Bao, S.; Xu, M. N doped FeP nanospheres decorated carbon matrix as an efficient electrocatalyst for durable lithium-sulfur batteries. *J. Colloid Interface Sci.* **2023**, *630*, 70–80. [[CrossRef](#)]
22. Hussain, N.; Li, M.; Tian, B.; Wang, H. Co₃Se₄ quantum dots as an ultrastable host material for potassium-ion intercalation. *Adv. Mater.* **2021**, *33*, 2102164. [[CrossRef](#)] [[PubMed](#)]
23. Mei, P.; Lee, J.; Pramanik, M.; Alshehri, A.; Kim, J.; Henzie, J.; Kim, J.H.; Yamauchi, Y. Mesoporous manganese phosphonate nanorods as a prospective anode for lithium-ion batteries. *ACS Appl. Mater. Interfaces* **2018**, *10*, 19739–19745. [[CrossRef](#)]
24. Xing, W.; Liu, C.; Li, T.; Zhang, T.; Han, J.; Wu, G. High-valence-state nickel-iron phosphonates with urchin-like hierarchical architecture for highly efficient oxygen evolution reaction. *J. Alloys Compd.* **2021**, *861*, 158614. [[CrossRef](#)]
25. Liu, X.; Zhuo, M.; Zhang, W.; Gao, M.; Liu, X.H.; Sun, B.; Wu, J. One-step ultrasonic synthesis of Co/Ni-catecholates for improved performance in oxygen reduction reaction. *Ultrason. Sonochem.* **2020**, *67*, 105179. [[CrossRef](#)]
26. Wang, P.; Lou, X.; Li, C.; Hu, X.; Yang, Q.; Hu, B. One-pot synthesis of Co-based coordination polymer nanowire for Li-ion batteries with great capacity and stable cycling stability. *Nano-Micro Lett.* **2018**, *10*, 19. [[CrossRef](#)] [[PubMed](#)]
27. Pan, G.-X.; Zhang, Y.-H.; Sun, P.-P.; Yu, X.; Gao, J.; Shi, F.-N. A brand-new bimetallic copper-lithium HEDP complex of fast ion migration as a promising anode for lithium ion batteries. *J. Mol. Struct.* **2020**, *1214*, 128223. [[CrossRef](#)]
28. Mei, P.; Pramanik, M.; Young, C.; Huang, Z.; Hossain, M.S.A.; Sugahara, Y.; Yamauchi, Y. Synthesis of mesostructured manganese phosphonate and its promising energy storage application. *J. Mater. Chem. A* **2017**, *5*, 23259–23266. [[CrossRef](#)]
29. Wang, L.; Wang, Z.; Xie, L.; Zhu, L.; Cao, X. An enabling strategy for ultra-fast lithium storage derived from micro-flower-structured NiX (X = O, S, Se). *Electrochim. Acta* **2020**, *343*, 136138. [[CrossRef](#)]
30. Zheng, F.; Yang, Y.; Chen, Q. High lithium anodic performance of highly nitrogen-doped porous carbon prepared from a metal-organic framework. *Nat. Commun.* **2014**, *5*, 5261. [[CrossRef](#)] [[PubMed](#)]
31. Lu, Y.; Yuan, L.; Peng, Q.; Qi, S.; Wang, L.; Chen, J.; Wang, Y.; Lv, L.-P.; Sun, W.; Wang, Y.; et al. A kind of Co-based coordination compounds with tunable morphologies and its Li-storage mechanism. *Electrochim. Acta* **2022**, *422*, 140565. [[CrossRef](#)]
32. An, T.; Wang, Y.; Tang, J.; Wang, Y.; Zhang, L.; Zheng, G. A flexible ligand-based wavy layered metal-organic framework for lithium-ion storage. *J. Colloid Interface Sci.* **2015**, *445*, 320–325. [[CrossRef](#)]
33. Guo, L.; Sun, J.; Sun, X.; Zhang, J.; Hou, L.; Yuan, C. Construction of 1D conductive Ni-MOF nanorods with fast Li⁺ kinetic diffusion and stable high-rate capacities as an anode for lithium ion batteries. *Nanoscale Adv.* **2019**, *1*, 4688–4691. [[CrossRef](#)]
34. Jin, J.; Zheng, Y.; Huang, S.-Z.; Sun, P.-P.; Srikanth, N.; Kong, L.B.; Yan, Q.; Zhou, K. Directly anchoring 2D NiCo metal-organic frameworks on few-layer black phosphorus for advanced lithium-ion batteries. *J. Mater. Chem. A* **2019**, *7*, 783–790. [[CrossRef](#)]
35. Cai, Y.; Wang, W.; Cao, X.; Wei, L.; Ye, C.; Meng, C.; Yuan, A.; Pang, H.; Yu, C. Synthesis of tostadas-shaped metal-organic frameworks for remitting capacity fading of Li-ion batteries. *Adv. Funct. Mater.* **2022**, *32*, 1209927. [[CrossRef](#)]
36. Shi, Y.; Zhu, G.; Guo, X.; Jing, Q.; Pang, H.; Zhang, Y. Three-dimensional MXene-encapsulated porous Ni-NDC nanosheets as anodes for enhanced lithium-ion batteries. *Nano Res.* **2022**, *16*, 2528–2535. [[CrossRef](#)]
37. Dong, C.; Xu, L. Cobalt- and cadmium-based metal-organic frameworks as high-performance anodes for sodium ion batteries and lithium ion batteries. *ACS Appl. Mater. Interfaces* **2017**, *9*, 7160–7168. [[CrossRef](#)]
38. Zheng, J.; Engelhard, M.H.; Mei, D.; Jiao, S.; Polzin, B.J.; Zhang, J.-G.; Xu, W. Electrolyte additive enabled fast charging and stable cycling lithium metal batteries. *Nat. Energy* **2017**, *2*, 17012. [[CrossRef](#)]
39. Li, G.; Yang, H.; Li, F.; Cheng, F.; Shi, W.; Chen, J.; Cheng, P. A coordination chemistry approach for lithium-ion batteries: The coexistence of metal and ligand redox activities in a one-dimensional metal-organic Material. *Inorg. Chem.* **2016**, *55*, 4935–4940. [[CrossRef](#)]

40. Chen, L.; Yang, W.; Wang, J.; Chen, C.; Wei, M. Hierarchical cobalt-based metal-organic framework for high-performance lithium-ion batteries. *Chem. Eur. J.* **2018**, *24*, 13362–13367. [[CrossRef](#)]
41. Zhang, F.; Du, M.; Miao, Z.; Li, H.; Dong, W.; Sang, Y.; Jiang, H.; Li, W.; Liu, H.; Wang, S. Oxygen vacancies and N-doping in organic-inorganic pre-intercalated vanadium oxide for high-performance aqueous zinc-ion batteries. *InfoMat* **2022**, *4*, e12346. [[CrossRef](#)]
42. Qi, X.-R.; Liu, Y.; Ma, L.-L.; Hou, B.-X.; Zhang, H.-W.; Li, X.-H.; Wang, Y.-S.; Hui, Y.-Q.; Wang, R.-X.; Bai, C.-Y.; et al. Delicate synthesis of quasi-inverse opal structural $\text{Na}_3\text{V}_2(\text{PO}_4)_3/\text{N-C}$ and $\text{Na}_4\text{MnV}(\text{PO}_4)_3/\text{N-C}$ as cathode for high-rate sodium-ion batteries. *Rare Met.* **2022**, *41*, 1637–1646. [[CrossRef](#)]
43. Shan, L.; Wang, Y.; Liang, S.; Tang, B.; Yang, Y.; Wang, Z.; Lu, B.; Zhou, J. Interfacial adsorption–insertion mechanism induced by phase boundary toward better aqueous Zn-ion battery. *InfoMat* **2021**, *3*, 1028–1036. [[CrossRef](#)]
44. Zheng, Z.; Li, P.; Huang, J.; Liu, H.; Zao, Y.; Hu, Z.; Zhang, Q. High performance columnar-like Fe_2O_3 @carbon composite anode via yolk@shell structural design. *J. Energy Chem.* **2020**, *41*, 126–134. [[CrossRef](#)]
45. Zou, G.; Hou, H.; Cao, X.; Ge, P.; Zhao, G.; Yin, D.; Ji, X. 3D hollow porous carbon microspheres derived from Mn-MOFs and their electrochemical behavior for sodium storage. *J. Mater. Chem. A* **2017**, *5*, 23550–23558. [[CrossRef](#)]
46. Jiang, Y.; Zou, G.; Hong, W.; Zhang, Y.; Zhang, Y.; Shuai, H.; Xu, W.; Hou, H.; Ji, X. N-rich carbon-coated Co_3S_4 ultrafine nanocrystals derived from ZIF-67 as an advanced anode for sodium-ion batteries. *Nanoscale* **2018**, *10*, 18786–18794. [[CrossRef](#)]
47. Guo, C.; Yang, J.; Cui, Z.; Qi, S.; Peng, Q.; Sun, W.; Lv, L.-P.; Xu, Y.; Wang, Y.; Chen, S. In-situ structural evolution analysis of Zr-doped $\text{Na}_3\text{V}_2(\text{PO}_4)_2\text{F}_3$ coated by N-doped carbon layer as high-performance cathode for sodium-ion batteries. *J. Energy Chem.* **2022**, *65*, 514–523. [[CrossRef](#)]
48. Nagmani; Kumar, A.; Puravankara, S. Optimizing ultramicroporous hard carbon spheres in carbonate ester-based electrolytes for enhanced sodium storage in half-/full-cell sodium-ion batteries. *Battery Energy* **2022**, *1*, 514–523. [[CrossRef](#)]
49. Wang, Z.; Cui, G.; Zheng, Q.; Ren, X.; Yang, Q.; Yuan, S.; Bao, X.; Shu, C.; Zhang, Y.; Li, L.; et al. Ultrafast Charge-Discharge Capable and Long-Life $\text{Na}_{3.9}\text{Mn}_{0.95}\text{Zr}_{0.05}\text{V}(\text{PO}_4)_3/\text{C}$ Cathode Material for Advanced Sodium-Ion Batteries. *Small* **2023**, *19*, e2206987. [[CrossRef](#)]

Disclaimer/Publisher’s Note: The statements, opinions and data contained in all publications are solely those of the individual author(s) and contributor(s) and not of MDPI and/or the editor(s). MDPI and/or the editor(s) disclaim responsibility for any injury to people or property resulting from any ideas, methods, instructions or products referred to in the content.